Metamorphosis of Heterostructured Surface-Mounted Metal–Organic Frameworks Yielding Record Oxygen Evolution Mass Activities

Shujin Hou, Weijin Li,* Sebastian Watzele, Regina M. Kluge, Song Xue, Shanshan Yin, Xinyu Jiang, Markus Döblinger, Alexander Welle, Batyr Garlyyev, Max Koch, Peter Müller-Buschbaum, Christof Wöll, Aliaksandr S. Bandarenka,* and Roland A. Fischer*

Materials derived from surface-mounted metal–organic frameworks (SURMOFs) are promising electrocatalysts for the oxygen evolution reaction (OER). A series of mixed-metal, heterostructured SURMOFs is fabricated by the facile layer-by-layer deposition method. The obtained materials reveal record-high electrocatalyst mass activities of ≈2.90 kA g^{-1} at an overpotential of 300 mV in 0.1 M KOH, superior to the benchmarking precious and non-precious metal electrocatalysts. This property is assigned to the particular in situ self-reconstruction and self-activation of the SURMOFs during the immersion and the electrochemical treatment in alkaline aqueous electrolytes, which allows for the generation of NiFe (oxy)hydroxide electrocatalyst materials of specific morphology and microstructure.

1. Introduction

Electrochemical water splitting offers an attractive means for producing renewable hydrogen fuel, which is promising for carbon-neutral energy provision schemes owing to its high energy density.[1–5] However, the main cause of low efficiency in this process is the anodic half-reaction,[6,7] namely, the oxygen evolution reaction (OER), which shows sluggish kinetics. Hence, exploring highly efficient and cost-effective earth-abundant electrocatalysts is a desirable solution to cope with these issues.[8] Non-noble electrocatalysts, such as transition-metal oxides, hydroxides, sulfides, and phosphides, have been regarded as promising alternatives. Among them, Ni-based and Fe-incorporated Ni-based compounds exhibit high OER activity in alkaline media.[9–13]

Metal oxo/hydroxo materials derived from surface-mounted metal–organic frameworks (SURMOFs) have shown promising OER performances due to the highly tuneable film thickness, controllable growth orientation and binder-free processing.[14–16] Thus, the layer-by-layer deposition of ultrathin SURMOFs on conductive substrates offers an effective strategy to design highly active

S. Hou, Dr. S. Watzele, R. M. Kluge, Dr. S. Xue, Dr. B. Garlyyev, Prof. A. S. Bandarenka
Physics of Energy Conversion and Storage
Physik-Department
Technische Universität München
James-Franck-Str. 1, 85748 Garching, Germany
E-mail: bandarenka@ph.tum.de

S. Hou, Dr. W. Li, Prof. A. S. Bandarenka, Prof. R. A. Fischer
Catalysis Research Center TUM
Ernst-Otto-Fischer-Straße 1, 85748 Garching, Germany
E-mail: wj.li@tum.de; roland.fischer@tum.de

Dr. W. Li, Prof. R. A. Fischer
Chair of Inorganic and Metal–Organic Chemistry
Department of Chemistry
Technische Universität München
Lichtenbergstraße 4, 85748 Garching, Germany

The ORCID identification number(s) for the author(s) of this article can be found under https://doi.org/10.1002/adma.202103218.

S. Yin, X. Jiang, Prof. P. Müller-Buschbaum
Lehrstuhl für Funktionelle Materialien
Physik-Department
Technische Universität München
James-Franck-Str. 1, 85748 Garching, Germany

Dr. M. Döblinger
Department of Chemistry
Ludwig-Maximilians-Universität München
Butenandtstr. 5–13 (E), 81377 München, Germany

Dr. A. Welle, Prof. C. Wöll
Institut für Funktionelle Grenzflächen (IFG)
Karlsruhe Nano Micro Facility (KNMF)
Karlsruher Institut für Technologie (KIT)
76021 Karlsruhe, Germany

M. Koch
Department of Chemistry
Technische Universität München
Lichtenbergstraße 4, 85748 Garching, Germany

Prof. P. Müller-Buschbaum
Heinz Maier-Leibnitz Zentrum (MLZ)
Technische Universität München
Lichtenbergstr. 1, 85748 Garching, Germany

**ADVANCED
SCIENCE NEWS**
www.advancedsciencenews.com

**ADVANCED
MATERIALS**
www.advmat.de

electrocatalysts and enables precise adjustment of defects and accessible active centres at the molecular level. Interestingly, heterostructured systems generally exhibit a higher catalytic activity than their uniformly structured counterparts, attributed to synergistic effects of the electrode structure/composition and interface properties.[17–21] Herein, we demonstrate taking advantage of both, the opportunities of SURMOF heterostructure growth and of their unique metamorphosis to yield metal oxo/hydroxo materials of special morphology and microstructure. We measured record oxygen evolution mass activities of ≈2.90 kA g^{-1} at the overpotential of 300 mV in 0.1 m KOH, superior to the benchmarking precious and nonprecious metal electrocatalysts. To the best of our knowledge, this is the highest reported mass activity for NiFe-based electrocatalysts.

SURMOFs have been reported to yield highly active electrocatalysts toward water oxidation, but the electrochemical stability or transformations and the origin of active species in MOF-based catalytic systems remain elusive.[22,23] Recent studies focus on the elucidation of the active species in MOF-based catalytic systems, and discover the presence of metal hydroxides in the electrochemically tested (SUR)MOF catalysts via a series of advanced physicochemical techniques.[24–27] Therefore, the stated active species were presumed to originate from MOF-derived metal hydroxides during the oxygen electrocatalytic process in alkaline electrolytes. Despite some recent efforts devoted to elucidate the catalytic species, an in-depth understanding of the transformation mechanisms and the structure–performance relationships remains open.

In this work, we use heterostructured NiFe-based SURMOFs composed of deprotonated terephthalic acid ([TA]$^{2-}$) linkers and exploit variants in structure and composition to optimize the OER performance. The experiments show that heterostructured SURMOFs undergo specific in situ reconstruction and self-activation process during the alkaline immersion and the electrochemical measurements, resulting in metal hydroxides and oxyhydroxides together with a partial leaching of the organic linkers. We propose using SURMOFs as precursors allowing for access to a parameter space of catalyst fabrication, which is beyond existing synthetic concepts.

2. Results and Discussion

The NiFe-based SURMOFs have been prepared through a stepwise layer-by-layer deposition process on functionalized gold substrates, as illustrated in Figure S1 in the Supporting Information. Three different types of samples have been prepared. The first type, heterostructured Ni|Fe-[TA]-SURMOFs, have been prepared using a two-step procedure. Initially, 15 layers of Ni-[TA] have been deposited on the gold substrate, followed by a deposition of 15 layers of Fe-[TA] on top. Note that "Ni|Fe" in the formula indicates the Ni-containing layers being the bottom layers and the Fe-containing layers being the top layers. The second type of sample is a mixed-phase NiFe-[TA]-SURMOFs prepared by simultaneous layer-by-layer deposition of both Ni- and Fe-layers in the presence of [TA]$^{2-}$. The third sample, Fe|Ni-[TA]-SURMOFs have been obtained by initially depositing 15 layers of Fe-[TA] followed by 15 layers of Ni-[TA]. More details are given in the experimental section. According to structural

engineering, heterostructures do not solely induce the electron transfer between different components to expose more active sites, but also facilitate the mass diffusion by rationally constructing well-defined nanostructures.[28,29] In this light, the three NiFe-based SURMOFs and 30-layer monometallic Ni-[TA]-SURMOFs are further investigated to explore their catalytic performance for water oxidation.

To accurately evaluate the electrocatalytic performance, the activity of as-prepared electrodes is normalized to the catalyst's mass and geometric surface area of the electrode, respectively.[30] Before and after the electrochemical measurement, the electrodes' mass loading is recorded by a quartz crystal microbalance (QCM). Note that in **Figure 1**A the mass loading of SURMOF electrodes dramatically decreases after OER activity measurements in 0.1 m KOH solution. This indicates that components of the SURMOFs partially leached out, and the SURMOFs are transformed into SURMOF derivatives. We will refer to the SURMOFs after electrochemical cycling as "Catalysts." Hence, the derivatives of Ni|Fe-[TA]-SURMOFs, NiFe-[TA]-SURMOFs, Fe|Ni-[TA]-SURMOFs, and Ni-[TA]-SURMOFs are in the following denoted as Ni|Fe-[TA]-Catalyst, NiFe-[TA]-Catalyst, Fe|Ni-[TA]-Catalyst and Ni-[TA]-Catalyst, respectively. As shown in Figure 1B,C and Figure S2A (Supporting Information), the Ni|Fe-[TA]-Catalyst records a remarkable current density of ≈2.90 kA g^{-1} at the overpotential of 300 mV, which is nearly 5, 10 and 12 times higher than the mass activities of NiFe-[TA]-Catalyst (≈0.58 kA g^{-1}), Fe|Ni-[TA]-Catalyst (≈0.28 kA g^{-1}), and Ni-[TA]-Catalyst (≈0.25 kA g^{-1}), respectively. Moreover, the same catalytic activity trend based on the geometric current density can be found in Figure S2C,D in the Supporting Information, reiterating the remarkable OER performance of Ni|Fe-[TA]-Catalyst. These results suggest that the heterogeneous structure constructed by rationally adjusting the arrangement of Ni and Fe-based SURMOFs has a significant influence on the OER electrocatalytic performance. The corresponding Tafel slopes are utilized to study OER kinetics (Figure 1D; Figure S2D, Supporting Information). In the case of mass activity, the Ni|Fe-[TA]-Catalyst exhibits the lowest Tafel slope of ≈44.3 mV dec^{-1} compared to NiFe-[TA]-Catalyst (≈54.2 mV dec^{-1}), Fe|Ni [TA] Catalyst (≈60.8 mV dec^{-1}), and Ni-[TA]-Catalyst (≈87.1 mV dec^{-1}), further verifying the better OER reaction kinetics of Ni|Fe-[TA]-Catalyst. As shown in Figure 1E, Figure S3 (Supporting Information), Tables S1 and S2 (Supporting Information), the Ni|Fe-[TA]-Catalyst achieves an activity of ≈2.90 kA g^{-1} at the overpotential of 300 mV, outperforming other most recent state-of-the-art OER electrocatalysts. Moreover, the electrocatalytic activity of the Fe-[TA]-Catalyst is shown in Figure S4 in the Supporting Information, exhibiting a low intrinsic activity of ≈0.029 kA g^{-1}. However, due to the unstable characteristics of FeOOH at high biases,[31,32] the polarization curve of the Fe-[TA]-Catalyst exhibits a declining trend at an increased number of cycles.

In the following, we utilize various ex situ and in situ techniques to shed light on the nature of the active surface species and the structural evolution of SURMOFs during the electrochemical treatment. Initially, QCM measurements are carried out to monitor the mass changes during the structural evolution of SURMOFs. As shown in Figure S5 in the Supporting Information, the mass loading on the QCM electrode decreases from ≈2.77 to ≈1.77 μg after the immersion in 0.1 m KOH
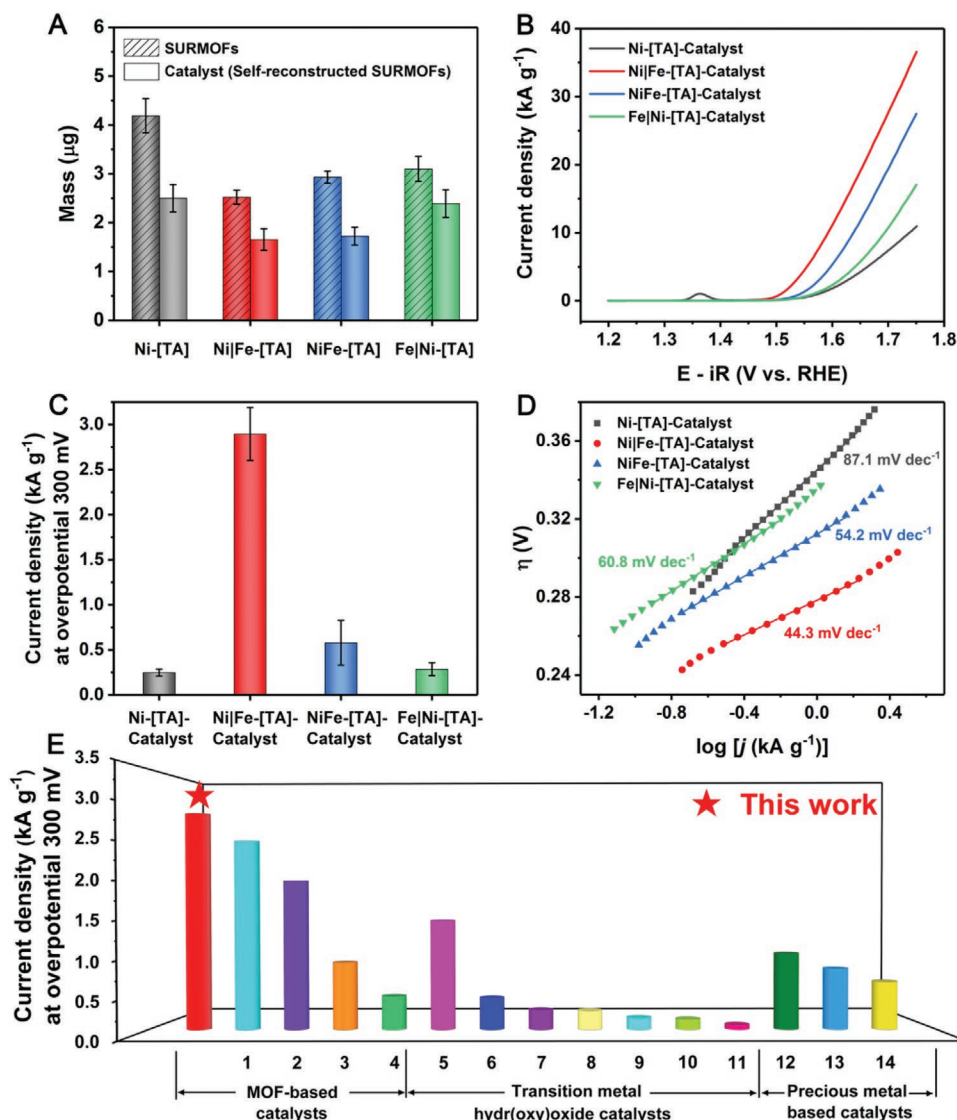
Figure 1. A) The mass loading of SURMOFs and Catalysts (self-reconstructed SURMOFs after electrochemical cycling) measured on the Au QCM electrodes. B) Polarization curves of Catalysts collected in 0.1 M O_2-saturated KOH with a scan rate of 5 mV s^{-1}. Current densities are normalized to the Catalyst mass. C) Comparison of mass activities at an overpotential of 300 mV for these Catalysts. D) The corresponding Tafel plots of all Catalysts. E) Comparison of the OER mass activity of Ni|Fe-[TA]-Catalyst with benchmarked data of state-of-the-art catalysts. 1–4) MOF-based catalysts, 5–11) transition metal (oxy)hydroxide catalysts and 12–14) precious-metal-based catalysts are compared at an overpotential of 300 mV: 1) 50Ni50Co-SURMOFD 10 cycles,[14] 2) lattice-strained 4.3%-MOF,[33] 3) NiFe-BTC-GNPs,[34] 4) [M(BDC)] nanosheets (M = Ni^{2+}, Co^{2+}),[35] 5) Cu–Ni–Fe hydr(oxy)oxide,[36] 6) NiFe-LDH@NiCu,[37] 7) δ-FeOOH NSs/nickel foam,[38] 8) NiFe LDH nanomesh,[39] 9) CoMn LDH,[40] 10) $Ni_{0.8}Fe_{0.2}O_xH_y$,[41] 11) γ-CoOOH nanosheets,[42] 12) $Rh_{22}Ir_{78}$/VXC,[43] 13) Ir-network,[44] and 14) Co–IrCu ONC/C.[45] For more details on the experimental conditions, please refer to Table S1 in the Supporting information.

solution for 3 min, revealing that the as-prepared SURMOFs are unstable in an alkaline medium. Meanwhile, the ex situ Raman and NMR spectra confirmed the rapid leaching of the organic linkers and the generation of FeOOH species during the 3 min KOH immersion process (Figures S6 and S7, Supporting Information). After that, cyclic voltammetry (CV) is performed to promote further the structural evolution of the SURMOFs (**Figure 2**A). It is found that the polarization curve of the first cycle shows an anodic peak in the potential range of 1.25–1.46 V versus the reversible hydrogen electrode (RHE). This increase in faradaic current can be assigned to the

oxidation of SURMOF species.[16,26] Furthermore, the oxidation current increases in a higher potential range (1.46–1.54 V), suggesting that more SURMOF species are oxidized. With the increasing number of cycles, a distinguishable redox couple peak corresponding to the reversible redox transition between Ni^{2+} and Ni^{3+} species can be observed.[16,46,47] Notably, both the Ni^{2+}/Ni^{3+} redox peak and the OER current gradually increase and stabilize after the 35th cycle. This can be ascribed to the continuous exposure of Ni^{2+}–Ni^{3+} species and an increasing number of accessible catalytically active sites. Therefore, it is meaningful to denote the SURMOFs after the electrochemical
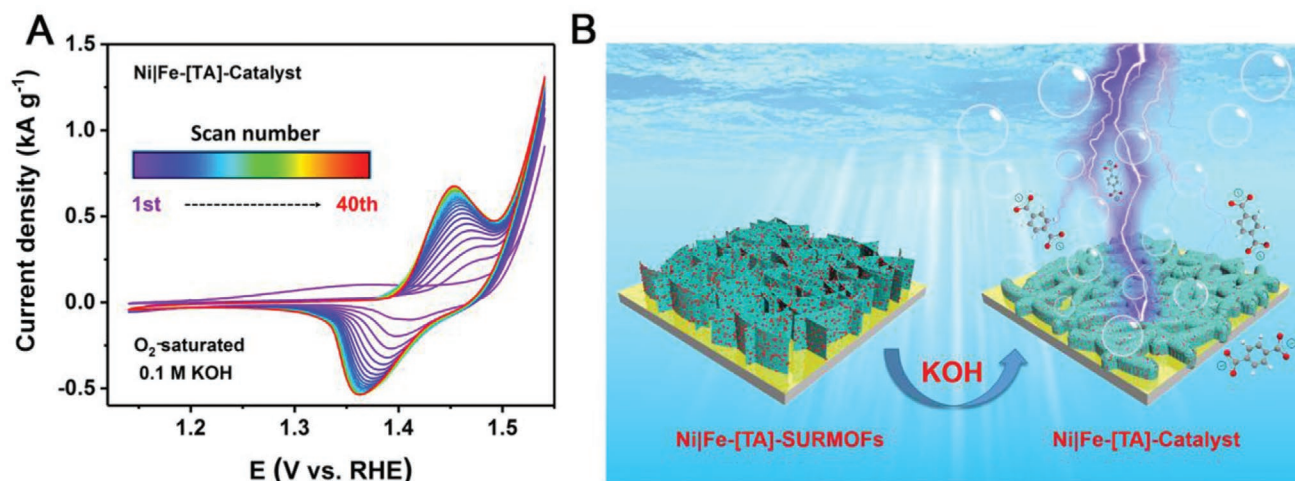
Figure 2. A) Cyclic voltammogram of Ni|Fe-[TA]-Catalyst electrode recorded with scan rate 20 mV s^{-1} for 40 cycles in 0.1 M KOH solution. B) Schematic illustration showing the transformation process of heterostructured SURMOFs into Catalysts in alkaline electrolyte.

cycling as "Catalysts." According to these facts, we propose a mechanism for the structural evolution of SURMOFs into Catalysts, as shown in Figure 2B. Heterostructured SURMOFs are undergoing an in situ self-reconstruction process in the alkaline electrolyte. In the case of the alkaline-unstable SURMOF thin films, the coordinate bonds between metal nodes and organic linkers can be dissociated in the KOH electrolyte, thereby leading to the replacements of organic linkers by the OH^{-}/H$_2$O. In this process of SURMOF metamorphosis, phase structural transition facilitates the generation of disordered NiFe hydroxides, which generally possess abundant defects. Subsequently, CV cycling accelerates the reconstruction and self-activation processes, leading to the exposure of a higher number/density of active sites, which significantly improve the OER activity.

From the electrochemical data, it becomes apparent that a change in composition takes place after electrochemical cycling. The increase in OER current implies a higher number of active sites being available. The latter translates into structural changes. To directly access the crystalline structure and orientation of the SURMOFs during this structural evolution, grazing-incidence wide-angle X-ray scattering (GIWAXS) is performed on these samples. **Figure 3** illustrates the 2D GIWAXS patterns and the corresponding line-cut profiles of the Ni|Fe-[TA]-SURMOFs, the Ni|Fe-[TA]-SURMOFs after 3 min immersion in 0.1 M KOH solution (denoted as KOH immersion), and the Ni|Fe-[TA]-Catalyst. In the 2D GIWAXS data (Figure 3A–C; Figure S9, Supporting Information), two significant diffraction rings at scattering vectors of q = 2.64 and 3.04 Å^{-1} are visible for all samples, which are dominated by the scattering signals of the QCM substrate. More importantly, two pronounced Bragg diffraction spots in the scattering patterns are present in the 2D GIWAXS data (Figure 3A,C), corresponding to the generation of crystalline phases on the as-prepared SURMOFs and its NiFe hydroxide derivatives, respectively.[35,48] These diffraction spots manifest a high degree of preferential crystallographic orientation pertaining to the substrate.[49] Furthermore, from cake-cuts of the GIWAXS patterns, the (010), (600), (1-10), and (210) Bragg peaks located at q = 2.93, 2.95, 2.98, and 3.09 Å^{-1}, respectively,

are present in the Ni|Fe-[TA]-SURMOFs (Figure 3D,E; Table S4, Supporting Information), indicating its high crystallinity. Note that these crystalline structures of the SURMOFs are destroyed after 3 min KOH-immersion procedure, as indicated by the loss of the (010), (600), (1-10), and (210) diffraction signals. After the electrochemical treatment, a new diffraction peak located at q = 2.72 Å^{-1} appears in the line-cut profile of Ni|Fe-[TA]-Catalyst (Figure 3E; Table S5, Supporting Information), corresponding to the (015) diffraction peak of NiFe layered double hydroxide (NiFe-LDH).[48] Additionally, a preferential orientation located at around χ = 34.5° with a broad orientation distribution can be observed for Ni|Fe-[TA]-SURMOFs (Figure 3F; Figure S10A, Supporting Information). In contrast, there is no orientation peak in the tube cut pattern of the Ni|Fe-[TA]-KOH immersion sample, indicating a structural collapse of high-order MOFs and the generation of amorphous NiFe hydroxide. On the Ni|Fe-[TA]-Catalyst, a sharp peak at χ = 45.4° with a narrow orientation distribution is detected in the tube cut pattern (Figure 3F; Figure S10C, Supporting Information). From these observations, one can conclude that the evolution process from the as-prepared SURMOFs to the Catalyst involves two steps. The first step includes the phase transition of crystalline SURMOFs into amorphous NiFe hydroxide during the KOH immersion treatment. Afterward, NiFe-layered double hydroxide (LDH) material with crystallographic orientation is generated after the electrochemical activation.

To elucidate the structural transformation of the SURMOFs, especially the existence of morphological structures during the derivation process, scanning electron microscopy (SEM), atomic force microscopy (AFM) and transmission electron microscopy (TEM) are performed on the freshly prepared samples. Interestingly, the heterostructures can be easily inferred from the hierarchical ultrathin nanosheet array and nanoclusters in Ni|Fe-[TA]-SURMOFs and Fe|Ni-[TA]-SURMOFs (Figures S12C and S14C, Supporting Information), where the ultrathin nanosheets represent Ni-[TA]-SURMOFs and nanoclusters are from Fe-[TA]-SURMOFs. A more detailed discussion is given in the Supporting Information. After the OER test, significant morphology changes are observed for all

**ADVANCED
SCIENCE NEWS**

www.advancedsciencenews.com

**ADVANCED
MATERIALS**

www.advmat.de
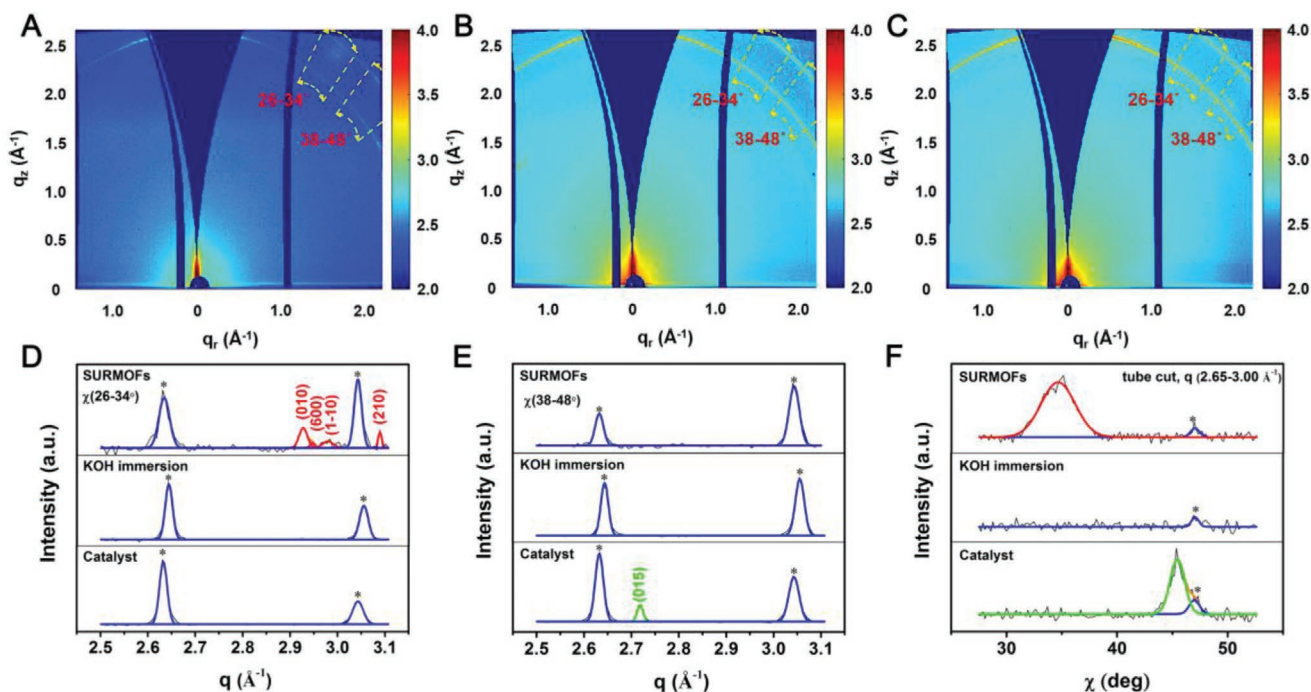
Figure 3. A–C) 2D GIWAXS data of the Ni|Fe-[TA]-SURMOFs in the as-prepared state (A), after 3 min immersion in a 0.1 M KOH solution (B) and after electrochemical cycling until the Ni|Fe-[TA]-Catalyst is obtained (C). D,E) Cake cuts performed at angles between $\chi = 26$–$34°$ (D) and 38–$48°$ (E) derived from the 2D GIWAXS data. F) Tube cuts in a q range of 2.65–3.00 Å^{-1}. All Peaks are fitted with Gaussian functions. The peaks denoted with a star (*) can be assigned to the diffraction peaks (blue lines) of the substrates. The red lines represent oriented Ni|Fe-[TA]-SURMOFs crystals and the green lines represent oriented NiFe layered-double-hydroxides crystals.

samples as shown in the SEM images (Figures S11D, S12D, S13D, and S14D, Supporting Information). These interconnected nanofiber networks, which cover the gold substrate, are derived from the nanosheet structures of the pristine SURMOFs after the OER test. Moreover, AFM images reveal the decreased roughness and thickness in these SURMOF derivatives compared with the initial SURMOF-coated electrodes (Figures S12E,F, S13E,F, and S14E,F and Table S6, Supporting Information), which provide further support for the reconstruction of the SURMOFs in the alkaline electrolyte. From the TEM image shown in **Figure 4**A, the ultrathin nanosheets can be observed in the Ni|Fe-[TA]-SURMOFs, corresponding to the 2D Ni-[TA]-SURMOFs. Benefiting from the unique ultrathin morphology, these nanosheets are embedded in a matrix of nanoparticles with uniform sizes, where the nanoparticles should be attributed to the Fe-[TA] according to the SEM image in Figure S12C in the Supporting Information. In Figure 4D, the TEM image of the Ni|Fe-[TA]-Catalyst shows a similar matrix of nanoparticles, however the nanosheets are not observable anymore, suggesting the structural transformation of SURMOFs after the OER test. The diffraction patterns of both samples show broad diffraction rings on a strong diffuse background, and the latter indicates a large amorphous material fraction. The d-values in the inset of Figure 4A are very similar with the structure of SURMOFs, while the d-values obtained from the stronger diffraction rings in inset of Figure 4D are in agreement with $Fe_{0.67}Ni_{0.33}OOH$ (PDF#00-014-0556). The high-resolution TEM image in Figure 4B further reveals the presence of nanosheets, whereas lattice fringes are not visible due to low

crystallinity and beam sensitivity. In addition, energy-dispersive X-ray spectroscopy (EDX) elemental mappings are used to study the elementary distribution of O, Fe, and Ni. In overlap elemental mappings of Fe and Ni (Figure 4C), the Fe signal is much stronger than the Ni, which is in good agreement with the heterostructures in Ni|Fe-[TA]-SURMOFs. After the OER test, EDX elemental mappings in STEM mode show the uniform distribution of O, Fe, and Ni in the Ni|Fe-[TA]-Catalyst (Figure 4F).

To gain deeper insight into the self-reconstruction process of heterostructured SURMOFs, time-of-flight secondary ion mass spectrometry (ToF-SIMS) is conducted to ascertain the evolution of chemical species at both surface and bulk of catalyst thin film. As representatively shown in **Figure 5**A,B for Ni|Fe-[TA]-SURMOFs, the intensity of the Fe$^+$ signal is much stronger than that of the Ni$^+$. The opposite trend in Fe$^+$ and Ni$^+$ signal intensities is found for Fe|Ni-[TA]-SURMOFs (Figure S17A,B, Supporting Information). This result can be ascribed to the achievement of well-designed heterostructures, e.g., the bottom-layer Ni-[TA] in Ni|Fe-[TA]-SURMOFs is covered by the top-layer Fe-[TA], leading to a stronger Fe-signal in the surface chemical mapping image. After the electrochemical activation, the signal ratio of Fe:Ni species significantly decreases from 16.5:1 to 1.98:1 when Ni|Fe-[TA]-SURMOFs are transformed into Ni|Fe-[TA]-Catalyst (Figure 5C,D; Table S7, Supporting Information). Therefore, it is reasonable to assume a self-reconstruction and re-distribution of Ni and Fe species in the pristine SURMOFs during the electrochemical treatment in alkaline media. In addition, ToF-SIMS depth profiles are measured to ascertain the distribution of C, Ni and Fe species

**ADVANCED
SCIENCE NEWS**

www.advancedsciencenews.com

**ADVANCED
MATERIALS**

www.advmat.de
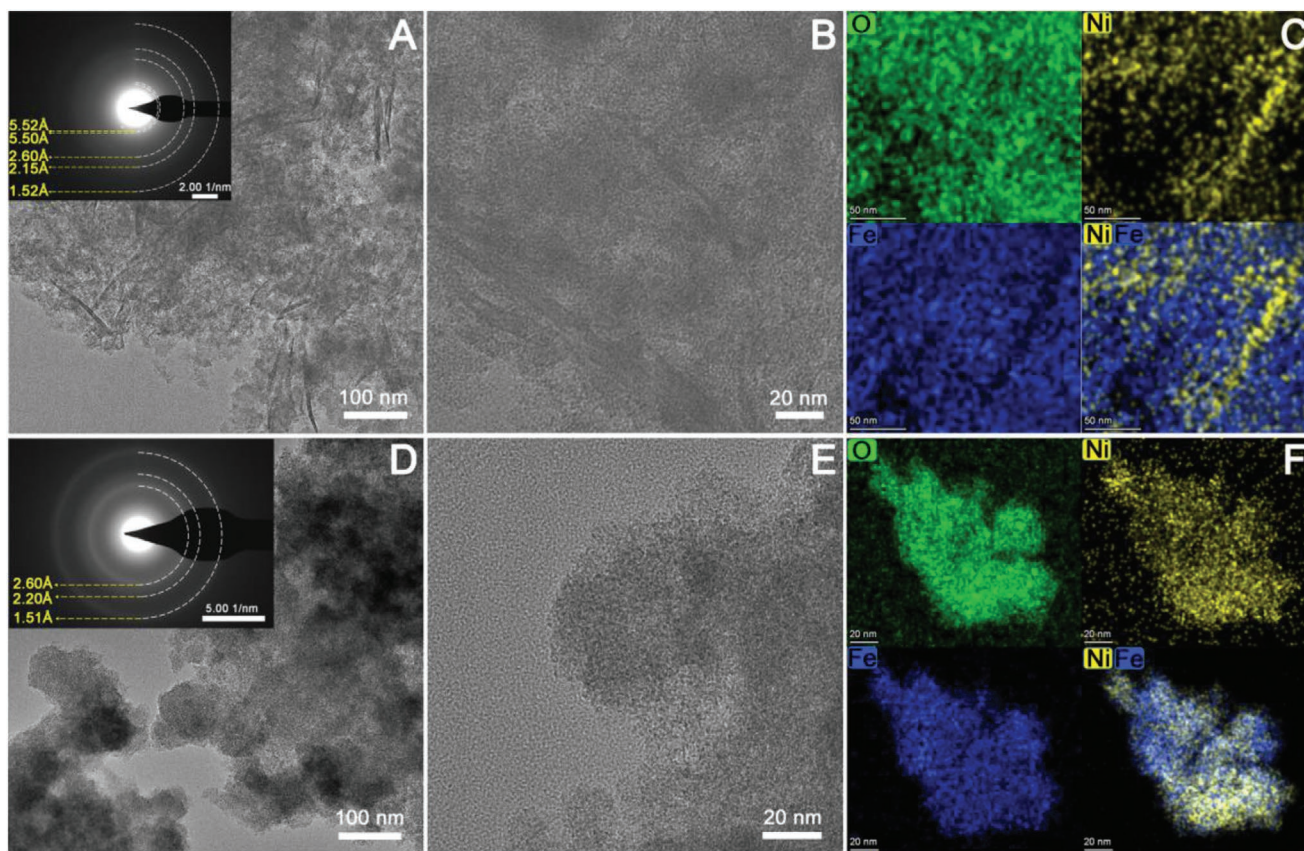
Figure 4. A,B) TEM and HRTEM images of Ni|Fe-[TA]-SURMOFs. The inset in (A) represents the selected-area electron diffraction (SAED) pattern. C) EDX elemental mappings in STEM mode of O, Fe, and Ni in Ni|Fe-[TA]-SURMOFs. D,E) TEM and HRTEM images of Ni|Fe-[TA]-Catalyst. The inset in (D) represents the SAED pattern. F) EDX elemental mappings in STEM mode of O, Fe, and Ni in Ni|Fe-[TA]-Catalyst.

in the bulk of SURMOFs and their derived Catalysts. For Ni|Fe-[TA]-SURMOFs, a Fe^+ signal can be detected in the initial 25 s. Afterward, the intensity rapidly increases to reach its maximum with a subsequent decrease as the sputtering further proceeds (Figure 5E). In comparison, the curve of Ni^+ signal lags behind that of Fe^+ signal, which is in good agreement with the heterostructural design concept. However, after electrochemical activation, the distribution of Ni- and Fe-species changes dramatically in the Ni|Fe-[TA]-Catalyst as shown in Figure 5F. Therefore, these observations coincide well with a self-reconstruction process.

X-ray photoelectron spectroscopy (XPS) analysis is performed to explore the surface chemical states and chemical composition of the as-prepared electrodes. As shown in **Figure 6A**, the C 1s spectrum of Ni|Fe-[TA]-SURMOFs deconvolutes into three peaks at binding energies of 284.8, 286.7, and 288.5 eV, which are attributed to C—C, C—O, and O=C—O bonds, respectively. These groups are expected since the organic linkers have been used in the synthesis process.[15,50,51] Corresponding peaks are also detected in the C 1s spectrum of Ni|Fe-[TA]-Catalyst, revealing the existence of residual organic linkers after OER. A new peak at 293 eV appears due to the presence of K^+, stemming from the KOH electrolyte.[50] Thus, the C 1s spectrum provides additional evidence for the residues of organic linkers in the derived catalysts. In the O 1s spectrum of the Ni|Fe-[TA]-SURMOF, two peaks at 531.7 and 532.9 eV can be assigned

to O=C—O groups and C—O bonds of the organic linkers (Figure 6B).[52,53] The intensity of both peaks significantly decreases after electrochemical activation. In contrast, the intensity of the other two peaks at 529.7 and 530.2 eV dramatically increases, corresponding to Ni(Fe)-oxygen bonds and Ni(Fe)-hydroxyl species, respectively.[50,54] This comparison demonstrates that organic linkers partially and gradually leaches into the electrolyte during the immersion in KOH and the electrochemical potential cycling. In addition, the relative content of Ni(Fe)-hydroxyl species increases after KOH immersion and electrochemical measurements, suggesting that a large number of Ni(Fe)-hydroxyl species are produced during electrochemical activation in KOH electrolyte (Table S8, Supporting Information). The high-resolution Fe 2p spectrum of Ni|Fe-[TA]-SURMOFs shows the Fe $2p_{3/2}$ and $2p_{1/2}$ peaks at 710.7 and 723.9 eV with two corresponding satellite peaks (Figure 6C), clearly indicating the presence of Fe^{3+}.[55] The Fe $2p_{3/2}$ peak of Ni|Fe-[TA]-Catalyst is positively shifted by ≈0.7 eV in comparison to the corresponding peak of the initial Ni|Fe-[TA]-SURMOFs, due to the dissociation of the organic linkers from the metal–organic coordination bond after the electrochemical process, resulting in a replacement of $[TA]^{2-}$ with OH^-/O^{2-}.[24,56] As such, the positively shifted binding energy indicates the decreased electron density in Fe^{3+} centers, owing to the change in coordination environment of Fe^{3+}.[24,56–58] Analogously, in the case of the Ni 2p spectrum of Ni|Fe-[TA]-SURMOFs (Figure 6D), two

ADVANCED
SCIENCE NEWS
www.advancedsciencenews.com

ADVANCED
MATERIALS
www.advmat.de
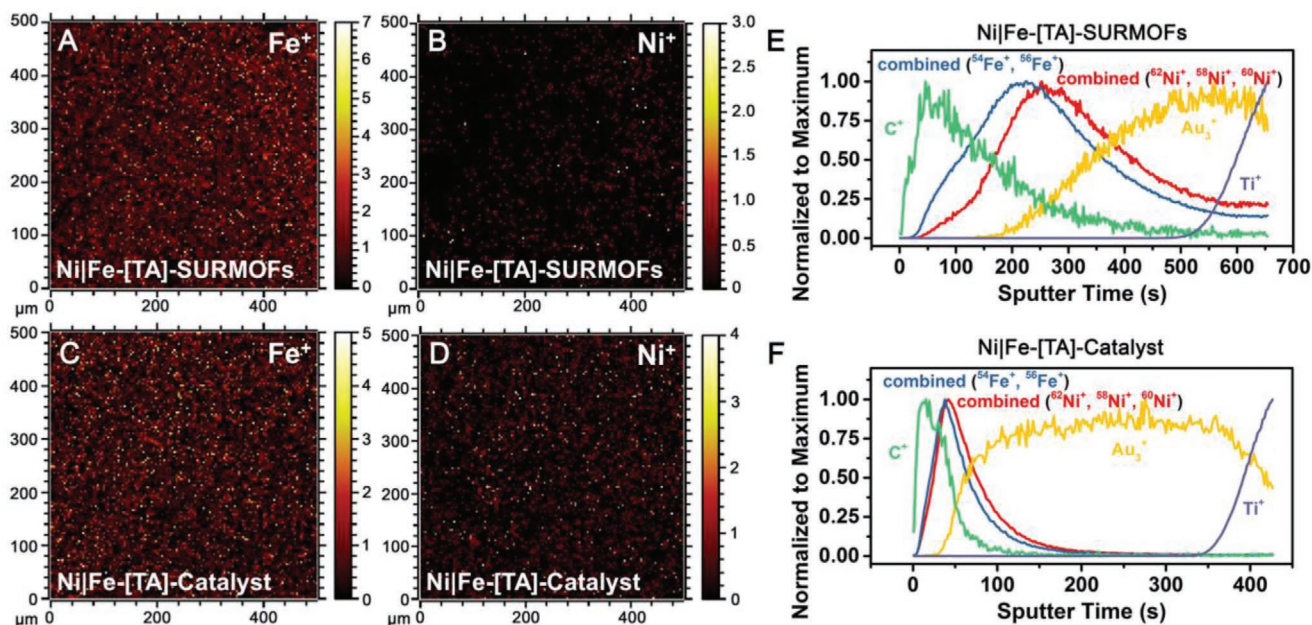
Figure 5. A–D) ToF-SIMS chemical mapping of Fe and Ni signals in the probed topmost layer of Ni|Fe-[TA]-SURMOFs and Ni|Fe-[TA]-Catalyst. E,F) Normalized ToF-SIMS intensities of C^+, Fe^+, Ni^+, Au^{3+}, and Ti^+ secondary ions along the depth profile of the Ni|Fe-[TA]-SURMOFs and Ni|Fe-[TA]-Catalyst. The Ti acts as an adhesion promoter underneath the gold electrode.

characteristic peaks are present at 856.2 and 874.1 eV, corresponding to Ni $2p_{3/2}$ and Ni $2p_{1/2}$, respectively, which can be assigned to Ni^{2+}, indicating the existence of pure Ni-[TA] SURMOFs.[59,60] Moreover, the intensity of Ni 2p signals significantly

increases after OER, indicating that more inner-layer Ni species diffused to the surface layer of catalysts. Initially, in Ni|Fe-[TA]-SURMOFs, the Ni-[TA] nanosheets are covered by large numbers of Fe-[TA] clusters. The structural evolution and
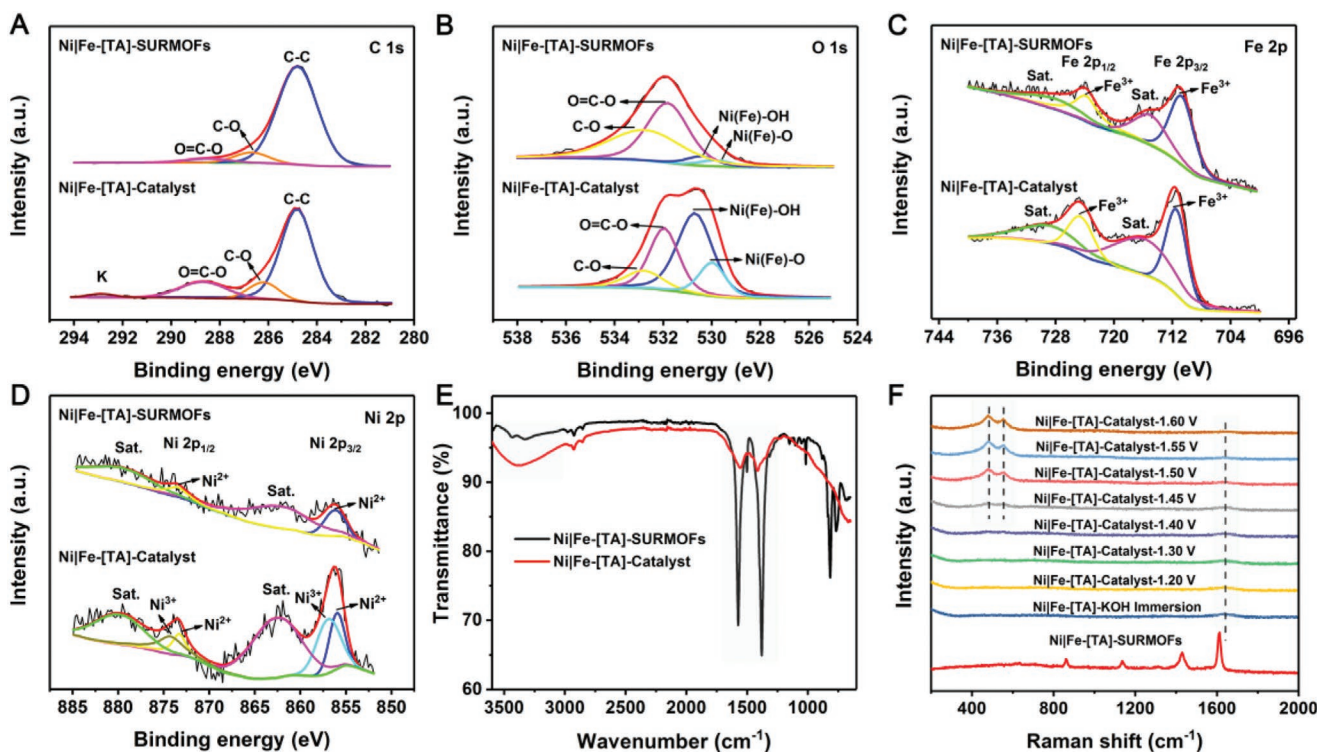
Figure 6. Spectral measurements on Ni|Fe-[TA]-SURMOFs and Ni|Fe-[TA]-Catalyst. a–d) High-resolution XPS spectra of C 1s (A), O 1s (B), Fe 2p (C), and Ni 2p (D). E) FT-IR spectra. F) In situ Raman spectra collected during the OER process in 0.1 м KOH within a low-wavenumber region of 200–2000 cm^{-1}.

**ADVANCED
SCIENCE NEWS**
www.advancedsciencenews.com

**ADVANCED
MATERIALS**
www.advmat.de

self-activation in alkaline solution expose more active Ni species to the surface of catalysts. The high-resolution Ni 2p XPS spectrum of Ni|Fe-[TA]-Catalyst differs from that of the pristine SURMOFs. The Ni $2p_{3/2}$ spectrum can be deconvoluted into two distinct peaks. A peak located at 856.0 eV is assigned to the Ni^{2+} species in $Ni(OH)_2/NiO_x$, where the binding energy is slightly higher than that of the Ni^{2+} peak in pure $Ni(OH)_2/NiO_x$ (≈855.4 eV) reported in the literature.[24,56,61,62] This higher binding energy found here indicates a lower electron density of Ni^{2+} centers in the derived Catalysts. In detail, the strong electron-withdrawing ability of the bridging $[TA]^{2-}$ linkers in the SURMOFs can induce a decrease of the electron density of the Ni^{2+}-centers via a weakened electron–electron repulsion between the p-orbitals ($2p^6$) of the own O atoms of linkers and the fully occupied π-symmetry (t_{2g}) d-orbitals of the Ni^{2+} species, leading to the increase in the binding energy of Ni^{2+}.[35,56] Accordingly, the residual $[TA]^{2-}$ linkers and Fe^{3+} dopants (Ni^{2+}-X-Fe^{3+}, X = O^{2-}, or $[TA]^{2-}$) play an important role in the positive shift of Ni $2p_{3/2}$ spectrum in $Ni(OH)_2/NiO_x$ phase. Another characteristic peak at a higher binding energy of ≈857.0 eV is ascribed to Ni^{3+} species. The lowest $Ni^{2+}:Ni^{3+}$ atomic ratio of 0.68:1 was obtained for Ni|Fe-[TA]-Catalyst. In comparison, for NiFe-[TA]-Catalyst and Fe|Ni-[TA]-Catalyst, a ratio of 1.08:1 and 2.49:1 is measured, respectively (Table S9, Supporting Information). This result indicates that more Ni^{3+} species are generated in Ni|Fe-[TA]-Catalyst during the potential cycling, which agrees with the trend of their OER performance. In the literature, it was reported that the high-oxidation state of Ni in NiFe-based double hydroxides can enhance the electrocatalytic activities toward water oxidation.[63]

Furthermore, Fourier transform infrared (FT-IR) spectroscopy results reveal that the chemical structures of these as-prepared SURMOFs drastically changed after the electrochemical process. As shown in Figure 6E, two peaks at 1571 and 1378 cm^{-1} assigned to the asymmetric stretching and symmetric stretching vibrations of the carboxyl groups in pristine Ni|Fe-[TA]-SURMOFs are observed, demonstrating the successful coordination of $[TA]^{2-}$ linkers with the metal ions in SURMOFs.[14,33,50] The intensity of the characteristic peaks of the carboxyl group significantly decreases after OER, suggesting partial leaching of organic linkers and the existence of residual $[TA]^{2-}$. Another broadened peak in the range of 3000–3550 cm^{-1} can be ascribed to O—H stretching vibration, which is characteristic for water molecules.[64]

Ex situ and in situ Raman spectroscopy are used to systematically investigate the structural self-reconstruction process from SURMOFs to catalysts during the OER process. Ni|Fe-[TA]-SURMOFs show four Raman shift peaks at 1610, 1430, 1140, and 863 cm^{-1} (Figure 6F), corresponding to coordinated organic linkers of pristine SURMOFs.[24] Interestingly, these peaks disappear after immersion into KOH for 3 min, indicating the destruction of the coordination of metal nodes and organic linkers after immersion in alkaline electrolyte. Meanwhile, a broad peak appears at ≈1637 cm^{-1}, which can be assigned to the uncoordinated carboxylate groups of $[TA]^{2-}$.[50] To further reveal the nature of the catalysts' active sites, an in situ electrochemical Raman spectroscopy is conducted. For potential below 1.40 V, the spectra remain unchanged. However, when the potential is increased to 1.45 V, two distinct Raman peaks evolve at around

482 and 554 cm^{-1}, which are attributed to Ni—O vibrations of the surface intermediate oxyhydroxide NiOOH.[65,66] The intensities of both peaks increase with increasing potentials and stabilize when the applied potential exceeded 1.50 V (Figure S20, Supporting Information). In addition, the intensity ratio of the two Ni—O Raman peaks (I_{554}/I_{482}) can be used to evaluate the structural disorder of NiOOH.[67,68] As shown in Figure S21 in the Supporting Information, in situ Raman experiment elucidates the high intensity ratio (≥0.84) of I_{554}/I_{482} in the OER potential region of 1.45–1.60 V versus RHE, suggesting abundant defects in the SURMOF derived NiOOH catalyst. Therefore, we can conclude that the generated Ni(Fe)-hydroxyl species, residual organic linkers and high oxidation state of Ni play a critical role in improving the OER performance.

The electroactive surface area (ECSA) of Catalysts and their density of active sites can be a decisive factor for their performance in the real application. However, the assessment of the ECSA is a nontrivial task in the case of metal oxides. In our previous work, we demonstrated an effective strategy to estimate the ECSA by analyzing the adsorption capacitance of OER species, which were reversibly adsorbed on the catalyst surface.[69] Therefore, electrochemical impedance spectroscopy (EIS) measurements are carried out at potentials close to the onset of the OER on the as-prepared catalysts. The EIS data were fitted and evaluated with the equivalent electric circuit (EEC) model shown in **Figure 7**A. The EEC used in this work, also known as Armstrong-Henderson EEC, accounts for the electrolyte resistance (R_s), a double layer impedance (Z_{dl}), a charge transfer resistance (R_{ct}), adsorption resistance (R_a), and the adsorption capacitance (C_a).[70,71] A representative Nyquist plot measured at 1.58 V is shown and fitted according to the EEC model (Figure 7A). As an outcome of the fit, the adsorption capacitances C_a for the different catalyst films are presented in Figure 7B, Figure S22B,D (Supporting Information) as a function of the applied potential. It can be seen that the C_a increases with increasing potentials, indicating the gradual activation of catalytically active centers (active sites). Remarkably, on Ni|Fe-[TA]-Catalyst, this activation occurs already at potentials lower than 1.50 V, while state-of-the-art NiFe catalysts do not show any increase in C_a at potentials below 1.55 V.[69] This is an additional indicator for the superior catalytic performance of this SURMOF derived catalyst. For a rough estimation of the ECSA, the adsorption capacitance is evaluated at 1.58 V and divided by the specific adsorption capacitance of NiFe at the same potential, i.e., C_a' (NiFe @ 1.58 V) ≈ 435 μF cm^{-2}. This yields an ECSA of ≈0.32 cm^2, which is ≈1.7 times higher than the geometric surface area of the substrate (≈0.196 cm^2). In other words, the synthesized Ni|Fe-[TA]-Catalyst has intrinsically a high density of active sites normalized to the geometric surface area, which is an additional reason for its outstanding activity. This is also reflected by significantly outperforming the Fe|Ni-[TA]-Catalyst and NiFe-[TA]-Catalyst, which show much lower C_a values, as can be seen in Figure 7C.

To further study the intrinsic electrocatalytic activity of prepared catalysts, the OER reaction kinetics are accessed by CV measurements at different temperatures. Noticeably, the temperature rises from 303.65 to 333.15 K results in an increased current density for the Ni|Fe-[TA]-Catalyst (Figure 7D), confirming the temperature dependence of OER performance. The

**ADVANCED
SCIENCE NEWS**

www.advancedsciencenews.com

**ADVANCED
MATERIALS**

www.advmat.de
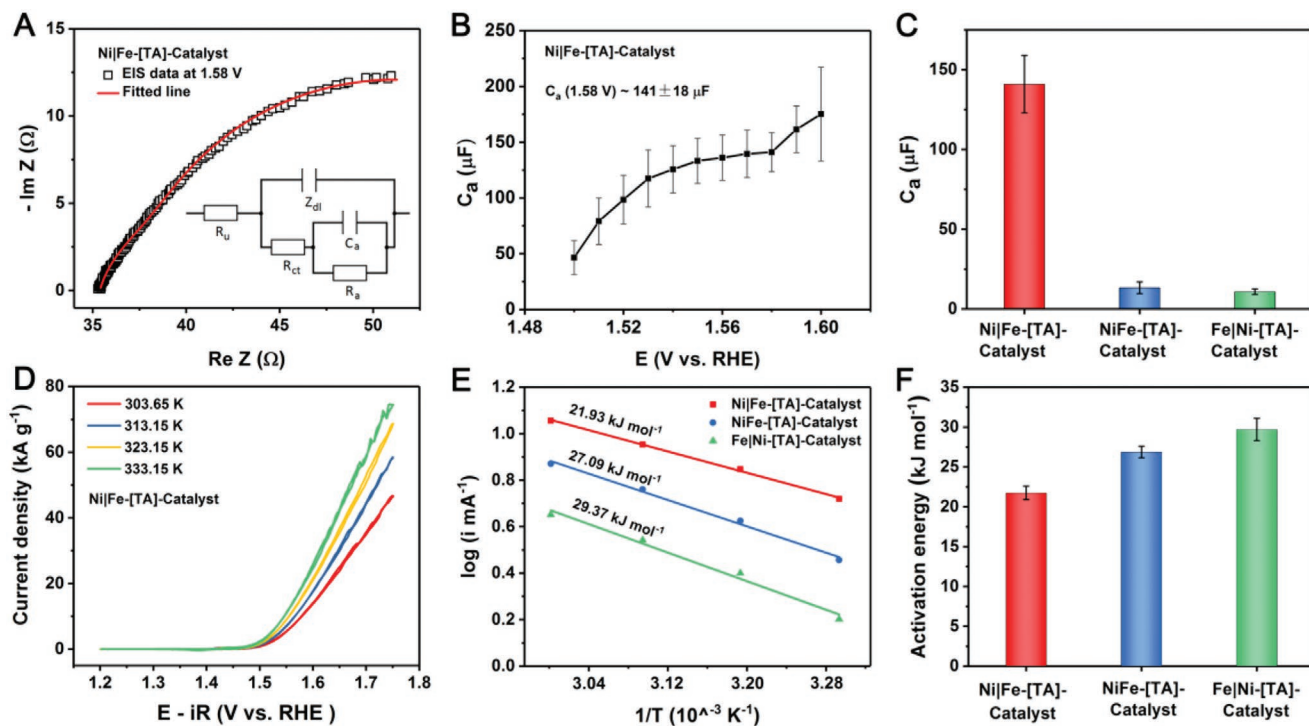
Figure 7. A) EIS data (black squares) of a Ni|Fe-[TA]-Catalyst electrode recorded at a potential of 1.58 V. The data were fitted (red line) according to the equivalent electric circuit shown in the inset. B) Adsorption capacitances of the Ni|Fe-[TA]-Catalyst electrode as a function of potential, recorded in a potential range from 1.50 to 1.60 V in Ar-saturated 0.1 M KOH. C) Comparison of the adsorption capacitances of the three different Catalysts. D) Polarization curves of Ni|Fe-[TA]-Catalyst electrode measured under various temperatures with a scan rate of 5 mV s^{-1} in O$_2$-saturated 0.1 M KOH. E) Arrhenius plot of the apparent exchange current as a function of temperature and F) calculated activation energy for all catalysts. The error bars were obtained from at least three independent experiments.

related Arrhenius plots extracted at the low current region for each of the different catalysts are linearly fitted as presented in Figure 7E. Their apparent activation energy is calculated via the slope of the Arrhenius plot.[72] Figure 7F displays the average apparent activation energy value ($\approx$21.73 kJ mol^{-1}) for Ni|Fe-[TA]-Catalyst, which is significantly smaller than that for NiFe-[TA]-Catalyst ($\approx$26.88 kJ mol^{-1}) and Fe|Ni-[TA]-Catalyst ($\approx$29.70 kJ mol^{-1}).

Chronopotentiometry experiments at three different current densities of 1.0, 2.0, and 3.0 kA g^{-1} confirm the high stability of the Ni|Fe-[TA] Catalyst for more than 34 h (Figure S23A, Supporting Information). Interestingly, the polarization curve after the 34-hour long-term test displays a slight increase in comparison with that before the long-term test (Figure S23B, Supporting Information). The redox peaks of Ni^{2+}/Ni^{3+} show a significantly positive shift, which can be due to the aging process.[68] The durability of the Ni|Fe-[TA]Catalyst is also examined via CVs. As shown in Figure S23C in the Supporting Information, similar trends of current increase and positive shift of redox peaks are obtained during the 400-cycle measurement, further confirming the aging process. Consistently, SEM, XRD, Raman, and XPS characterizations are performed to investigate the chemical properties of Ni|Fe-[TA]-Catalyst after the long-term test. In Figure S24 in the Supporting Information, the similar interconnected nanofiber networks can be found from the SEM image and no distinct XRD peak presents in the GIXRD pattern. Two peaks in the Raman spectra appear at

around 478 and 545 cm^{-1}, corresponding to Ni—O vibrations of the NiOOH. XPS analysis displays that partial organic links and abundant metal hydroxides construct the SURMOF derivatives. These pieces of evidence reveal the excellent structural and catalytic stability.

3. Conclusion

We have developed a facile strategy to prepare highly active LDH-type electrocatalysts of unique morphology and microstructure by reconstruction and self-activation of heterostructured SURMOFs. A series of ex situ and in situ experiments are carried out to reveal the details of the structural evolution process. The results confirm that KOH immersion and electrochemical potential cycling transform the alkaline-unstable NiFe heterostructured SURMOFs into electrocatalytically active derivatives. This transformation is characterized by the partial leaching of organic linkers and the generation of NiFe hydroxides/oxyhydroxides. Among the series of evaluated SURMOF derived catalysts in this study, the Ni|Fe-[TA]-Catalyst, which is formed from heterostructured Ni|Fe-[TA]-SURMOFs, shows the highest OER activity with a mass activity of $\approx$2.90 kA g^{-1} at an overpotential of 300 mV. We ascribe this excellent performance to the unique crystalline–amorphous phase obtained, which features a high content of Ni species in a higher oxidation state, a large electroactive surface area and a low apparent activation

energy. In this work, we do not only study the origin of catalytic activity for SURMOF-derived materials systematically, but we also show a promising route to design and fabricate high-efficiency electrocatalysts via the in situ reconstruction of heterostructured SURMOFs in alkaline electrolytes. In summary, our results suggest SURMOF technology to provide a novel parameter space LDH-type electrocatalyst fabrication to be further exploited and holds promise for further OER efficiency optimizations. More variations in the SURMOF fabrication can be envisaged, also including different electrode substrate materials and 3D shaped structures, which all-together may cause different kinds of kinetically controlled morphology transformation, structural metamorphosis, and self-activation.

Supporting Information

Acknowledgements

Conflict of Interest

The authors declare no conflict of interest.

Data Availability Statement

Research data are not shared.

Keywords

[1] Q. Zhang, E. Uchaker, S. L. Candelaria, G. Cao, *Chem. Soc. Rev.* **2013**, *42*, 3127.
[2] T. R. Cook, D. K. Dogutan, S. Y. Reece, Y. Surendranath, T. S. Teets, D. G. Nocera, *Chem. Rev.* **2010**, *110*, 6474.
[3] D. Wu, K. Kusada, S. Yoshioka, T. Yamamoto, T. Toriyama, S. Matsumura, Y. Chen, O. Seo, J. Kim, C. Song, S. Hiroi, O. Sakata, T. Ina, S. Kawaguchi, Y. Kubota, H. Kobayashi, H. Kitagawa, *Nat. Commun.* **2021**, *12*, 1145.
[4] H. Mistry, A. S. Varela, S. Kühl, P. Strasser, B. R. Cuenya, *Nat. Rev. Chem.* **2016**, *1*, 16009.
[5] H. Zhang, J. Nai, L. Yu, X. W. Lou, *Joule* **2017**, *1*, 77.
[6] M. Dincă, Y. Surendranath, D. G. Nocera, *Proc. Natl. Acad. Sci. USA* **2010**, *107*, 10337.
[7] S. Laha, Y. Lee, F. Podjaski, D. Weber, V. Duppel, L. M. Schoop, F. Pielnhofer, C. Scheurer, K. Müller, U. Starke, K. Reuter, B. V. Lotsch, *Adv. Energy Mater.* **2019**, *9*, 1803795.
[8] W. T. Hong, M. Risch, K. A. Stoerzinger, A. Grimaud, J. Suntivich, Y. Shao-Horn, *Energy Environ. Sci.* **2015**, *8*, 1404.
[9] F. Dionigi, P. Strasser, *Adv. Energy Mater.* **2016**, *6*, 1600621.
[10] L.-A. Stern, L. Feng, F. Song, X. Hu, *Energy Environ. Sci.* **2015**, *8*, 2347.
[11] Y. Guo, T. Park, J. W. Yi, J. Henzie, J. Kim, Z. Wang, B. Jiang, Y. Bando, Y. Sugahara, J. Tang, Y. Yamauchi, *Adv. Mater.* **2019**, *31*, 1807134.
[12] H. Zhang, W. Zhou, J. Dong, X. F. Lu, X. W. Lou, *Energy Environ. Sci.* **2019**, *12*, 3348.
[13] J. Zhao, J. J. Zhang, Z. Y. Li, X. H. Bu, *Small* **2020**, *16*, 2003916.
[14] W. Li, S. Watzele, H. A. El-Sayed, Y. Liang, G. Kieslich, A. S. Bandarenka, K. Rodewald, B. Rieger, R. A. Fischer, *J. Am. Chem. Soc.* **2019**, *141*, 5926.
[15] W. Li, S. Xue, S. Watzele, S. Hou, J. Fichtner, A. L. Semrau, L. Zhou, A. Welle, A. S. Bandarenka, R. A. Fischer, *Angew. Chem., Int. Ed.* **2020**, *59*, 5837.
[16] S. Begum, T. Hashem, M. Tsotsalas, C. Wöll, M. H. Alkordi, *Energy Technol.* **2019**, *7*, 1900967.
[17] F. Malara, A. Minguzzi, M. Marelli, S. Morandi, R. Psaro, V. Dal Santo, A. Naldoni, *ACS Catal.* **2015**, *5*, 5292.
[18] C. C. McCrory, S. Jung, J. C. Peters, T. F. Jaramillo, *J. Am. Chem. Soc.* **2013**, *135*, 16977.
[19] Y. Guo, J. Tang, H. Qian, Z. Wang, Y. Yamauchi, *Chem. Mater.* **2017**, *29*, 5566.
[20] R. Subbaraman, D. Tripkovic, D. Strmcnik, K.-C. Chang, M. Uchimura, A. P. Paulikas, V. Stamenkovic, N. M. Markovic, *Science* **2011**, *334*, 1256.
[21] S. Xue, R. W. Haid, R. M. Kluge, X. Ding, B. Garlyyev, J. Fichtner, S. Watzele, S. Hou, A. S. Bandarenka, *Angew. Chem., Int. Ed.* **2020**, *59*, 10934.
[22] Z. Xue, K. Liu, Q. Liu, Y. Li, M. Li, C.-Y. Su, N. Ogiwara, H. Kobayashi, H. Kitagawa, M. Liu, G. Li, *Nat. Commun.* **2019**, *10*, 5048.
[23] L. Heinke, C. Wöll, *Adv. Mater.* **2019**, *31*, 1806324.
[24] Q. Qian, Y. Li, Y. Liu, L. Yu, G. Zhang, *Adv. Mater.* **2019**, *31*, 1901139.
[25] M. Liu, L. Kong, X. Wang, J. He, X. H. Bu, *Small* **2019**, *15*, 1903410.
[26] W. Zheng, M. Liu, L. Y. S. Lee, *ACS Catal.* **2019**, *10*, 81.
[27] S. Zhao, C. Tan, C.-T. He, P. An, F. Xie, S. Jiang, Y. Zhu, K.-H. Wu, B. Zhang, H. Li, J. Zhang, Y. Chen, S. Liu, J. Dong, Z. Tang, *Nat. Energy* **2020**, *5*, 881.
[28] G. Zhao, K. Rui, S. X. Dou, W. Sun, *Adv. Funct. Mater.* **2018**, *28*, 1803291.
[29] A. R. Akbashev, L. Zhang, J. T. Mefford, J. Park, B. Butz, H. Luftman, W. C. Chueh, A. Vojvodic, *Energy Environ. Sci.* **2018**, *11*, 1762.
[30] J. Kibsgaard, I. Chorkendorff, *Nat. Energy* **2019**, *4*, 430.
[31] D. Y. Chung, P. P. Lopes, P. Farinazzo Bergamo Dias Martins, H. He, T. Kawaguchi, P. Zapol, H. You, D. Tripkovic, D. Strmcnik, Y. Zhu, S. Seifert, S. Lee, V. R. Stamenkovic, N. M. Markovic, *Nat. Energy* **2020**, *5*, 222.
[32] S. Zou, M. S. Burke, M. G. Kast, J. Fan, N. Danilovic, S. W. Boettcher, *Chem. Mater.* **2015**, *27*, 8011.
[33] W. Cheng, X. Zhao, H. Su, F. Tang, W. Che, H. Zhang, Q. Liu, *Nat. Energy* **2019**, *4*, 115.

[34] P. Thangavel, M. Ha, S. Kumaraguru, A. Meena, A. N. Singh, A. M. Harzandi, K. S. Kim, *Energy Environ. Sci.* **2020**, *13*, 3447.

[35] S. Zhao, Y. Wang, J. Dong, C.-T. He, H. Yin, P. An, K. Zhao, X. Zhang, C. Gao, L. Zhang, J. Lv, J. Wang, J. Zhang, A. M. Khattak, N. A. Khan, Z. Wei, J. Zhang, S. Liu, H. Zhao, Z. Tang, *Nat. Energy* **2016**, *1*, 16184.

[36] Z. Cai, L. Li, Y. Zhang, Z. Yang, J. Yang, Y. Guo, L. Guo, *Angew. Chem., Int. Ed.* **2019**, *58*, 4189.

[37] Y. Zhou, Z. Wang, Z. Pan, L. Liu, J. Xi, X. Luo, Y. Shen, *Adv. Mater.* **2019**, *31*, 1806769.

[38] B. Liu, Y. Wang, H. Q. Peng, R. Yang, Z. Jiang, X. Zhou, C. S. Lee, H. Zhao, W. Zhang, *Adv. Mater.* **2018**, *30*, 1803144.

[39] J. Xie, J. Xin, R. Wang, X. Zhang, F. Lei, H. Qu, P. Hao, G. Cui, B. Tang, Y. Xie, *Nano Energy* **2018**, *53*, 74.

[40] F. Song, X. Hu, *J. Am. Chem. Soc.* **2014**, *136*, 16481.

[41] M. B. Stevens, L. J. Enman, A. S. Batchellor, M. R. Cosby, A. E. Vise, C. D. M. Trang, S. W. Boettcher, *Chem. Mater.* **2017**, *29*, 120.

[42] J. Huang, J. Chen, T. Yao, J. He, S. Jiang, Z. Sun, Q. Liu, W. Cheng, F. Hu, Y. Jiang, Z. Pan, S. Wei, *Angew. Chem., Int. Ed.* **2015**, *54*, 8722.

[43] H. Guo, Z. Fang, H. Li, D. Fernandez, G. Henkelman, S. M. Humphrey, G. Yu, *ACS Nano* **2019**, *13*, 13225.

[44] A. W. Jensen, G. W. Sievers, K. D. Jensen, J. Quinson, J. A. Arminio-Ravelo, V. Brüser, M. Arenz, M. Escudero-Escribano, *J. Mater. Chem. A* **2020**, *8*, 1066.

[45] T. Kwon, H. Hwang, Y. J. Sa, J. Park, H. Baik, S. H. Joo, K. Lee, *Adv. Funct. Mater.* **2017**, *27*, 1604688.

[46] M. W. Louie, A. T. Bell, *J. Am. Chem. Soc.* **2013**, *135*, 12329.

[47] L. Trotochaud, S. L. Young, J. K. Ranney, S. W. Boettcher, *J. Am. Chem. Soc.* **2014**, *136*, 6744.

[48] F. Dionigi, Z. Zeng, I. Sinev, T. Merzdorf, S. Deshpande, M. B. Lopez, S. Kunze, I. Zegkinoglou, H. Sarodnik, D. Fan, A. Bergmann, J. Drnec, J. F. Araujo, M. Gliech, D. Teschner, J. Zhu, W. X. Li, J. Greeley, B. R. Cuenya, P. Strasser, *Nat. Commun.* **2020**, *11*, 2522.

[49] A. Z. Chen, M. Shiu, J. H. Ma, M. R. Alpert, D. Zhang, B. J. Foley, D. M. Smilgies, S. H. Lee, J. J. Choi, *Nat. Commun.* **2018**, *9*, 1336.

[50] W. Li, F. Li, H. Yang, X. Wu, P. Zhang, Y. Shan, L. Sun, *Nat. Commun.* **2019**, *10*, 5074.

[51] Y. Shi, Y. Yu, Y. Liang, Y. Du, B. Zhang, *Angew. Chem., Int. Ed.* **2019**, *58*, 3769.

[52] J. Chen, P. Zhuang, Y. Ge, H. Chu, L. Yao, Y. Cao, Z. Wang, M. O. L. Chee, P. Dong, J. Shen, M. Ye, P. M. Ajayan, *Adv. Energy Mater.* **2019**, *29*, 1903875.

[53] Z. Xue, Y. Li, Y. Zhang, W. Geng, B. Jia, J. Tang, S. Bao, H.-P. Wang, Y. Fan, Z.-w. Wei, Z. Zhang, Z. Ke, G. Li, C.-Y. Su, *Adv. Energy Mater.* **2018**, *8*, 1801564.

[54] Q. Zhang, N. M. Bedford, J. Pan, X. Lu, R. Amal, *Adv. Energy Mater.* **2019**, *9*, 1901312.

[55] Z. Cai, D. Zhou, M. Wang, S. M. Bak, Y. Wu, Z. Wu, Y. Tian, X. Xiong, Y. Li, W. Liu, S. Siahrostami, Y. Kuang, X. Q. Yang, H. Duan, Z. Feng, H. Wang, X. Sun, *Angew. Chem., Int. Ed.* **2018**, *57*, 9392.

[56] W. He, H.-M. Gao, R. Shimoni, Z.-Y. Lu, I. Hod, *ACS Appl. Energy Mater.* **2019**, *2*, 2138.

[57] F. Kong, W. Zhang, L. Sun, L. Huo, H. Zhao, *ChemSusChem* **2019**, *12*, 3592.

[58] J. Y. Chen, L. Dang, H. Liang, W. Bi, J. B. Gerken, S. Jin, E. E. Alp, S. S. Stahl, *J. Am. Chem. Soc.* **2015**, *137*, 15090.

[59] D. Zhu, C. Guo, J. Liu, L. Wang, Y. Du, S. Z. Qiao, *Chem. Commun.* **2017**, *53*, 10906.

[60] P. Wen, P. Gong, J. Sun, J. Wang, S. Yang, *J. Mater. Chem. A* **2015**, *3*, 13874.

[61] L. Trotochaud, J. K. Ranney, K. N. Williams, S. W. Boettcher, *J. Am. Chem. Soc.* **2012**, *134*, 17253.

[62] S. L. Candelaria, N. M. Bedford, T. J. Woehl, N. S. Rentz, A. R. Showalter, S. Pylypenko, B. A. Bunker, S. Lee, B. Reinhart, Y. Ren, S. P. Ertem, E. B. Coughlin, N. A. Sather, J. L. Horan, A. M. Herring, L. F. Greenlee, *ACS Catal.* **2017**, *7*, 365.

[63] O. Diaz-Morales, I. Ledezma-Yanez, M. T. M. Koper, F. Calle-Vallejo, *ACS Catal.* **2015**, *5*, 5380.

[64] F. L. Li, P. Wang, X. Huang, D. J. Young, H. F. Wang, P. Braunstein, J. P. Lang, *Angew. Chem., Int. Ed.* **2019**, *58*, 7051.

[65] B. S. Yeo, A. T. Bell, *J. Phys. Chem. C* **2012**, *116*, 8394.

[66] S. Lee, K. Banjac, M. Lingenfelder, X. Hu, *Angew. Chem., Int. Ed.* **2019**, *58*, 10295.

[67] S. Lee, L. Bai, X. Hu, *Angew. Chem., Int. Ed.* **2020**, *59*, 8072.

[68] S. Klaus, Y. Cai, M. W. Louie, L. Trotochaud, A. T. Bell, *J. Phys. Chem. C* **2015**, *119*, 7243.

[69] S. Watzele, P. Hauenstein, Y. Liang, S. Xue, J. Fichtner, B. Garlyyev, D. Scieszka, F. Claudel, F. Maillard, A. S. Bandarenka, *ACS Catal.* **2019**, *9*, 9222.

[70] A. Alobaid, C. Wang, R. A. Adomaitis, *J. Electrochem. Soc.* **2018**, *165*, J3395.

[71] A. C. Garcia, T. Touzalin, C. Nieuwland, N. Perini, M. T. M. Koper, *Angew. Chem., Int. Ed.* **2019**, *58*, 12999.

[72] J. R. Swierk, S. Klaus, L. Trotochaud, A. T. Bell, T. D. Tilley, *J. Phys. Chem. C* **2015**, *119*, 19022.